Photoluminescence behavior and visible light photocatalytic activity of ZnO, ZnO/ZnS and ZnO/ZnS/α-Fe$_2$O$_3$ nanocomposites

Gaurav HITKARI, Sandhya SINGH, Gajanan PANDEY

Sophisticated Instrumentation Laboratory, Department of Applied Chemistry,
School for Physical Science, Babasaheb Bhimrao Ambedkar University, Lucknow-226025 (U.P.), India

Abstract: In order to achieve effective, economic, and easily achievable photocatalyst for the degradation of dye methyl orange (MeO), ZnO, ZnO/ZnS and ZnO/ZnS/α-Fe$_2$O$_3$ nanocomposites were prepared by simple chemical synthetic route in the aqueous medium. Phase, crystallinity, surface structure and surface behavior of the synthesized materials were determined by X-ray diffraction (XRD) and Brunauer−Emmett−Teller analysis (BET) techniques. XRD study established formation of good crystalline ZnO, ZnO/ZnS and ZnO/ZnS/α-Fe$_2$O$_3$ nanomaterials. By using intensity of constituent peaks in the XRD pattern, the compositions of nanocomposites were determined. From the BET analysis, the prepared materials show mesoporous behavior, type IV curves along with H4 hysteresis. The ZnO/ZnS/α-Fe$_2$O$_3$ composite shows the largest surface area among three materials. From the UV−visible spectra, the band gap energy of the materials was determined. Photoluminescence spectra (PL) were used to determine the emission behavior and surface defects in the materials. In PL spectra, the intensity of UV peak of ZnO/ZnS is lowered than that of ZnO while in case of ZnO/ZnS/α-Fe$_2$O$_3$, the intensity further decreased. The visible emission spectra of ZnO/ZnS increased compared with ZnO while in ZnO/ZnS/α-Fe$_2$O$_3$ it is further increased compared with ZnO/ZnS. The as-synthesized materials were used as photocatalysts for the degradation of dye MeO. The photo-degradation data revealed that the ZnO/ZnS/α-Fe$_2$O$_3$ is the best photocatalyst among three specimens for the degradation of dye MeO. The decrease of intensity of UV emission peak and the increase of intensity of visible emission cause the decrease of recombination of electrons and holes which are ultimately responsible for the highest photocatalytic activity of ZnO/ZnS/α-Fe$_2$O$_3$.

Key words: nanocomposite; ZnO; ZnS; α-Fe$_2$O$_3$; calcination; optical properties; photocatalytic activity

1 Introduction

With the development of industry and economy, environmental problems have become more and more vigorous in recent years [1]. Organic contaminants, which are resistant to environmental degradation, thus capable of remaining in the environment for a long period of time, are more injurious to living organism [2,3]. The semiconductor photocatalysis has emerged as one of the most promising technologies for environmental remediation because it removes waste from the environment without producing secondary pollutants. Since it is ultra-violet as well as solar light driven, nontoxic in nature, effective and economical, thus it attracted great attention in recent years [4,5]. The operation of photocatalysis process by semiconductor materials is an easy and effective technique for eliminating a wide variety of organic contaminants [6,7]. Due to high excitation binding energy (60 meV) at room temperature, large direct band gap (3.37 eV), environmental stability, non-toxicity and low cost, ZnO is considered as a suitable photocatalyst for photodegradation of organic contaminants in ultra violet (UV) as well as visible region [8,9]. On exposure of UV−visible radiation, ZnO is photo-excited and positive holes (h^+_{VB}) in the valence band and negative electrons (e_{CB}) in the conduction band generate. The generated electron–hole pairs either recombine or are captured by other molecules, such as water or oxygen, forming reactive oxygen species (ROS) such as hydroxyl radical ($\bullet$OH) and superoxide radical anion ($\bullet O_2^-$). Here h^+_{VB} reacts with water to produce hydroxyl radicals ($\bullet$OH), whilst the e_{CB} reacts with O_2 to form superoxide radical anions ($\bullet O_2^-$) and hydrogen peroxide (H_2O_2). The latter can also generate hydroxyl radicals ($\bullet$OH). These

ROS can destroy the structure of various organic pollutants, leading to the formation of carbon dioxide and water which are non-toxic for the environment [10].

The photocatalytic utility of powdered nano-materials has two practical limitations: first the separation of fine particles after the treatment and recycling of the photocatalyst and the second low photo-efficiency. Photocatalytic activity of wide band gap materials entirely depends on ultraviolet (UV) irradiation and restricts expense of solar energy, thus limits efficiency in sunlight [11]; however, the enhancement of photocatalytic activity under visible light illumination is highly desired. For example, wide band gap energy of ZnO is suitable for absorption of UV light; however, it is too large to absorb visible light. Since the UV radiation contributes only 5% to sunlight, the use of ZnO in sunlight has limited photocatalytic application. A number of manipulations, such as doping transition metal ions [12,13] and merging of narrow band gap semiconducting materials [14] have been employed to achieve visible region activity. In this regard, many research works have been focused on ZnO modified with metallic elements to improve its photocatalytic performance. Further, the low doping ability of metals to ZnO restricts its photocatalytic application [15]. The photocatalytic improvements have been achieved by addition of SnO_2 [16], CdS [17] and GaN [18], a large number of binary composites such as Ag/ZnO [19], ZnO/CuS [20], ZnO/ZnS [21] and ZnS/CuS [22] and a small number of ternary nanocomposites such as TiO_2-SiO_2-Ag [23] and $Ag_2S-ZnO-ZnS$ [24]. Existence of defect states in ZnO creates defect energy levels between valance band and conduction band. These defect states act as trap centers for photogenerated electron and holes, thus slowing down the rate of recombination of electrons and holes [25]. Moreover, defect states are manipulated by impurities doping [10]. A number of theoretical reports revealed that the band gap of ZnO/ZnS can be engineered to fall in visible range [26]. SAHA et al [27] reported that in core-shell ZnO/ZnS, keeping core diameter of ZnO constant, the band gap decreased, as the shell thickness of ZnS increased. PANDEY et al [28] reported that band gap of colloidal zinc oxysulfide is dependent on the sulfur composition and band gap (E_g) value of 2.7 could be achieved when sulfur composition reaches 0.4 in $ZnO_{1-x}S_x$. Although a large number of reports are available on mixed semiconductor heterostructures, however, to the best of our knowledge, detailed optical study on ZnO/ZnS and $ZnO/ZnS/\alpha-Fe_2O_3$ composites and their use as a photocatalyst for degradation of dye under visible light irradiation is still lacking.

In this work, the influence of the thermal treatment on the properties of ZnO, ZnO/ZnS and $ZnO/ZnS/\alpha-Fe_2O_3$ composites and their photo-degradation efficiency for methyl orange were investigated.

2 Experimental

2.1 Materials

Analytical grade zinc nitrate hexahydrate ($Zn(NO_3)_2·6H_2O$), urea ($CO(NH_2)_2$), thiourea ($CS(NH_2)_2$), ferric hydroxide ($Fe(OH)_3$) (anhydrous) and methyl orange were purchased from Merck, India, and used without further purification. Deionized water was used as a solvent. All the glassware was cleaned by concentrated acid. The dried glassware was used in all the experiments.

2.2 Synthesis of ZnO, ZnO/ZnS and ZnO/ZnS/ $\alpha-Fe_2O_3$

In a typical synthesis, 3.00 g $CO(NH_2)_2$ and 5.00 g $Zn(NO_3)_2·6H_2O$ were dissolved in 100 mL ultrapure water and stirred at 80 °C for 2 h on the digital magnetic stirrer. The as-prepared precipitate was cooled-down naturally and filtrated. The precipitate was dried at 80 °C in the electric oven. ZnO nanoparticles (NPs) were obtained after calcination of dried precipitate in a muffle furnace at 600 °C for 0.5 h. The as-prepared ZnO NPs (0.02 mol) were mixed with 0.01 mol thiourea in 100 mL deionized water under constant magnetic stirring at 80 °C for 0.5 h. The product was filtered, washed several times with deionized water, dried at 80 °C in the electric oven and heated in muffle furnace at 600 °C for 0.5 h to obtain ZnO/ZnS nanocomposite. 0.485 g ZnO/ZnS nanocomposite was added into 100 mL of 0.5 mmol/L ($Fe(OH)_3$) solution with stirring at 80 ºC in magnetic stirrer for 30 min. The product was cooled at room temperature, filtered, washed with deionized water, dried at 80 °C and heated in muffle furnace at 600 °C for 0.5 h to obtain $ZnO/ZnS/\alpha-Fe_2O_3$.

2.3 Characterization

The XRD patterns of as-prepared ZnO, ZnO/ZnS and $ZnO/ZnS/\alpha-Fe_2O_3$ nanocomposites were recorded on a Pananalytical's X'Pert Pro X-ray diffraction equipment in the 2θ range from 20° to 80° with a step size of 0.025°. Scanning electron microscope (SEM) images of the products were observed on a JEOL6490 LB equipment. Transmission electron microscope (TEM) images of the products were observed on a JEOL JEM 200 CX equipment. The scanning electron micrographs were obtained at an operating voltage of 3 kV. The particle size distribution of the materials was observed on Zetasizer Nano Series ZS 90 equipment. Brunauer−Emmett−Teller (BET) analysis of all the materials was carried out on a BELSORP MINI (II) equipment.

Photoluminescence spectral studies of the materials were carried out on a spectrofluorometer (Perkin Elmer LS 55). UV−visible spectra were recorded in absorption mode with a carry 100 spctrophotometer in the wavelength range of 200−800 nm.

2.4 Photocatalytic activity

The photocatalytic activity of as-prepared ZnO, ZnO/ZnS and ZnO/ZnS/α-Fe$_2$O$_3$ materials was evaluated by photodegradation of methyl orange under visible light exposure in a photocatalytic chamber. 200 mg ZnO was first dispersed in 100 mL of 50×10^{-6} (mass fraction) MeO solution and stirred for 30 min in the dark condition in order to achieve the adsorption−desorption equilibrium. The solution was irradiated by using Xe lamp (500 W) and a 420 nm cutoff filter was used as a visible light source in a photocatalytic chamber. During irradiation, the solution was agitated using a magnetic stirrer, and air was bubbled into the reaction medium to provide a constant supply of oxygen. After desired time interval, an aliquot of the solution was isolated, centrifuged and its absorbance was measured on UV−visible spectrophotometer to calculate the degradation. The same procedure was also repeated for ZnO/ZnS and ZnO/ZnS/α-Fe$_2$O$_3$ composites. The photocatalytic degradation efficiency (η) was calculated using the following equation:

$$\eta = \frac{(C_0 - C_t)}{C_0} \times 100\% = \frac{(A_0 - A_t)}{A_0} \times 100\% \qquad (1)$$

where C_0 is the initial concentration, C_t is the concentration at time t, A_0 is the initial absorbance of the dye solution, and A_t is the absorbance after irradiation at a particular time.

3 Results and discussion

The XRD patterns were recorded to analyze the phase, crystal structure and purity of as-synthesized ZnO, ZnO/ZnS, and ZnO/ZnS/α-Fe$_2$O$_3$ nanocomposites. All the diffraction peaks in the XRD patterns of as-synthesized materials, obtained by reaction of zinc nitrate in the presence of urea in an aqueous medium (Fig. 1(a)) are readily indexed to hexagonal wurtzite ZnO (JCPDS No. 80−0075, a=0.3253 nm, c=0.5209 nm) with space group $p63mc$. From Fig. 1(a), it is evident that the as-synthesized material, obtained by calcination of precipitate at 600 °C, is pure ZnO phase. Furthermore, it is obvious from the diffraction pattern that the XRD peaks are intense and broadened, indicating that ZnO material with good crystalline and small size is formed. Figure 1(b) represents the nanocomposite formed after addition of NH$_2$CSNH$_2$ to ZnO in an aqueous medium. In this XRD pattern, apart from wurtzite ZnO, additional

peaks appearing at 2θ values of 28.7°, 48.1° and 56.2°, which are respectively (111), (220) and (311) planes of ZnS phase (JCPDS No. 05−0566), indicate that the above material is ZnO/ZnS composite. With addition of Fe(OH)$_3$ to ZnO/ZnS, some additional peaks are also observed in the XRD pattern. In addition to ZnO/ZnS peaks, the other peaks appearing at 2θ values of 33.1°, 35.4°, 41.8° and 58.2°, correspond to (104), (110), (113) and (018) planes respectively are characteristics of α-Fe$_2$O$_3$ phase (Fig. 1(c)). The existence of three components implies that the ZnO/ZnS/α-Fe$_2$O$_3$ composite has successfully been prepared by the three-step chemical reaction. In the XRD pattern, the intensities of diffraction peaks for various constituents indicate the ratios of constituents. In the XRD pattern of ZnO/ZnS, using intensities of (111) peak of ZnS and (101) peak of ZnO, the compositions of ZnS and ZnO were found to be 17.91% and 82.09% (mass fraction), respectively. Similarly, in the XRD pattern of ZnO/ZnS/α-Fe$_2$O$_3$, using intensities of (111) peak of ZnS, (101) peak of ZnO and (104) peak of α-Fe$_2$O$_3$, the compositions of ZnS, ZnO and α-Fe$_2$O$_3$ were found to be 7.55%, 51.52% and 40.93% (mass fraction), respectively. The average crystallite size (D) has been determined from the Debye−Scherrer formula [29]

$$D = \frac{0.9\lambda}{\beta \cos \theta} \qquad (2)$$

where D is the crystallites size, λ the wavelength, β is the full width at half maxima (FWHM) and θ is the Bragg's diffraction angle. The average crystallite sizes of ZnO, ZnO/ZnS and ZnO/ZnS/α-Fe$_2$O$_3$ particles were estimated to be 120, 84 and 110 nm, respectively.
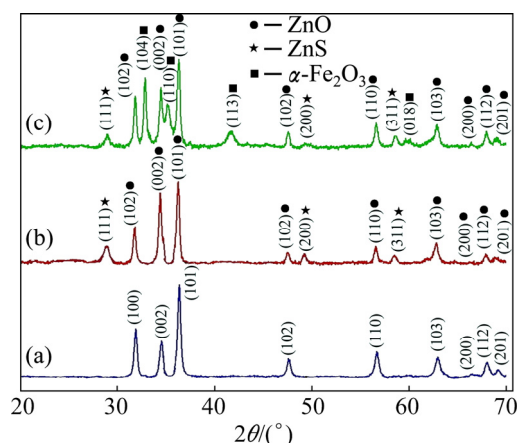

Fig. 1 XRD patterns of ZnO (a), ZnO/ZnS (b) and ZnO/ZnS/α-Fe$_2$O$_3$ (c) composites prepared at 600 °C

The Brunauer−Emmett−Teller (BET) analysis was applied to calculating the surface areas of ZnO, ZnO/ZnS and ZnO/ZnS/α-Fe$_2$O$_3$ nanocomposites. The surface areas (a_p) of ZnO, ZnO/ZnS and ZnO/ZnS/α-Fe$_2$O$_3$

nanocomposites were found to be 14.37, 15.96 and 17.0 m²/g, respectively. The pore volumes (V_p) of ZnO, ZnO/ZnS and ZnO/ZnS/α-Fe$_2$O$_3$ nanocomposites were found to be 8.06, 8.84 and 9.03 cm³/g, respectively. From the above data, it is obvious that as the surface area increases, the corresponding pore volume increases.

Figure 2 shows the nitrogen adsorption−desorption isotherm curves for ZnO, ZnO/ZnS and ZnO/ZnS/α-Fe$_2$O$_3$ composites which are typical type IV curves along with H4 hysteresis curve according to the IUPAC classification and show the presence of mesoporous phases [30].
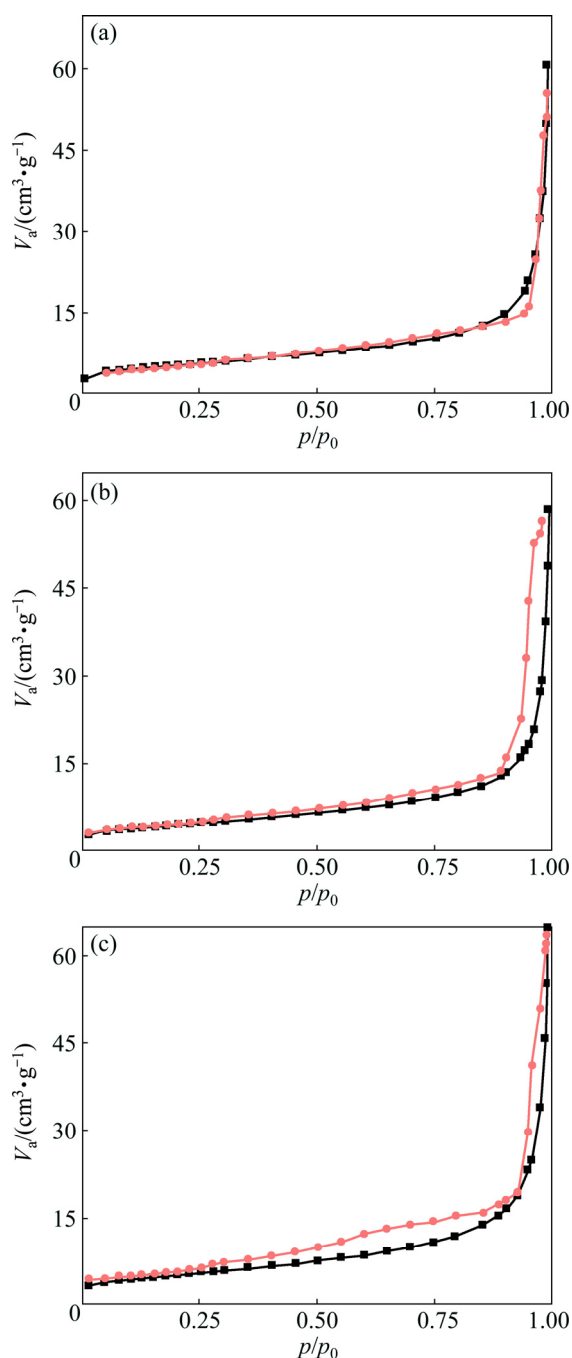
Fig. 2 N$_2$ adsorption−desorption isotherms of ZnO (a), ZnO/ZnS (b) and ZnO/ZnS/α-Fe$_2$O$_3$ (c) nanocomposites

The structural, morphological and compositional investigations of the as-synthesized products were carried out by SEM and EDX analysis. Figure 3(a) shows the SEM image of ZnO, formed by heating the precipitate, obtained by reaction of Zn(NO$_3$)$_2$·6H$_2$O in the presence of urea in an aqueous medium. In the SEM image, sheet-like structures with (25±5) nm in thickness and (100±60) nm in diameter are observed. Though there is variation in dimension (diameter), the thickness of sheets is almost uniform. The corresponding EDX pattern (Fig. 3(b)) shows that the molar fractions of Zn and O are 59.0% and 35.6%, respectively, which indicate that Zn/O molar ratio in the product is almost 1:1, suggesting that the material is composed of Zn and O elements in molar ratio 1:1.

The SEM image of ZnO/ZnS composites is shown in Fig. 3(c). It is obvious from Fig. 3(c) that, the morphology of ZnO/ZnS composite is similar to that of ZnO; however, there is a wide variation in the dimension of sheets (in the range of 50−300 nm). The corresponding EDX spectrum shows the molar fractions of Zn, S and O being 49.0%, 14.6%, and 32.5%, respectively (Fig. 3(d)), indicating that the nanocomposite is composed of ZnO and ZnS.

In the SEM image (Fig. 3(e)), needle-like acicular morphologies of the ZnO/ZnS/α-Fe$_2$O$_3$ nanocomposites with the thickness of 40−60 nm and length of (150±50) nm have been formed. In the corresponding EDX spectrum (Fig. 3(f)), the molar fractions of Zn, O, S and Fe (42.0%, 29.2%, 13.6% and 9.5%, respectively) exhibit the formation of ZnO/ZnS/α-Fe$_2$O$_3$ nanocomposite. From the SEM image, it is obvious that although the presence of ZnS has no effect on the morphology of ZnO, the presence of α-Fe$_2$O$_3$ completely changes the morphology from nano-sheet to acicular nanostructure.

The particle size distribution of ZnO, ZnO/ZnS, and ZnO/ZnS/α-Fe$_2$O$_3$ materials was studied on Zetasizer APS and the results are shown in Fig. 4. For particle size distribution study, the materials were mixed in DMSO and sonicated. From particle size distribution curves, it is obvious that size distribution of ZnO is fair; however, for ZnO/ZnS and ZnO/ZnS/α-Fe$_2$O$_3$ materials the size distribution is wide. These results are in agreement with SEM analysis discussed above.

The optical property of the synthesized materials was examined by recording UV−visible absorption spectrum which is significant for illustrating the optical absorption property as well as band gap energy of the semiconducting materials. Figure 5(a) shows the absorption spectra of ZnO, ZnO/ZnS, and ZnO/ZnS/α-Fe$_2$O$_3$ materials. In the absorption spectra of ZnO nanosheet, the absorbance peak appears at 397 nm which corresponds to the excitonic peak of ZnO NPs [31]. The
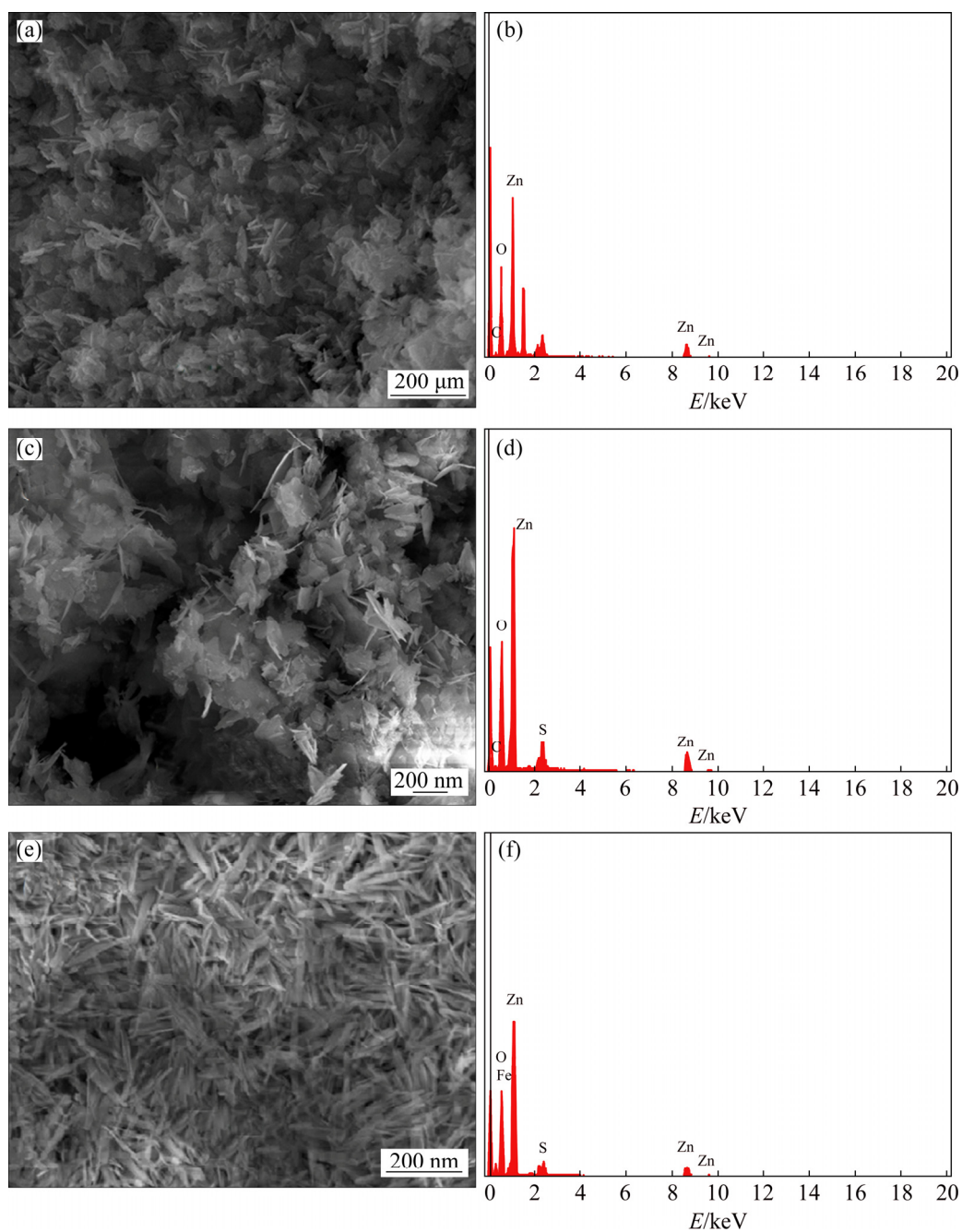
Fig. 3 SEM images (a, c, e) and EDX spectra (b, d, f) of ZnO (a, b), ZnO/ZnS (c, d) and ZnO/ZnS/α-Fe₂O₃ (e, f) nanocomposites
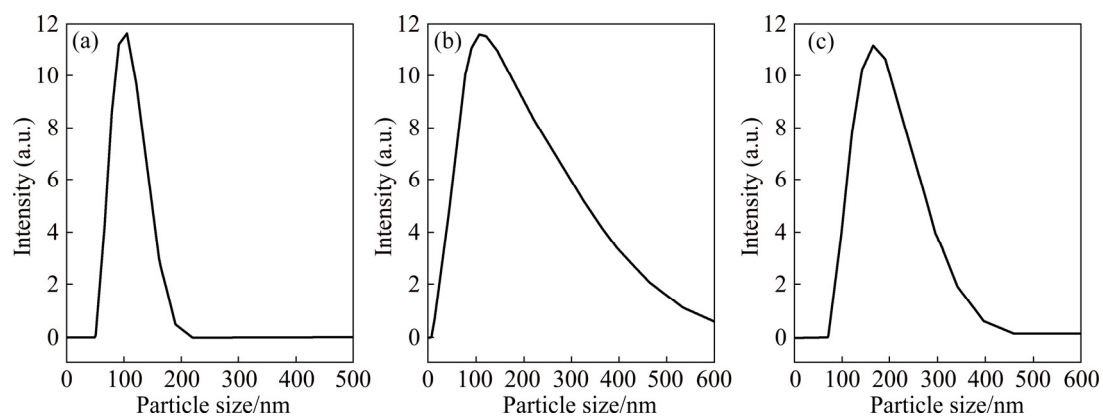
Fig. 4 Particle size distributions of ZnO (a), ZnO/ZnS (b) and ZnO/ZnS/α-Fe₂O₃ (c) materials
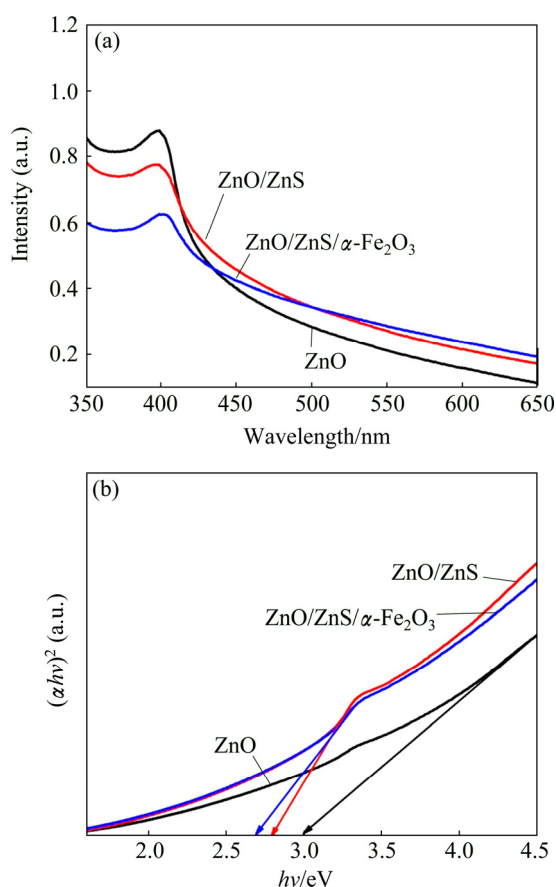
Fig. 5 UV−visible spectra (a) and band gap energy (b) of ZnO, ZnO/ZnS and ZnO/ZnS/α-Fe$_2$O$_3$ nanocomposites

maximum absorption is red shifted in ZnO/ZnS and further in case of ZnO/ZnS/α-Fe$_2$O$_3$ composites. The red shifting in the materials is due to the quantum confinement effect and the packing of material of ZnO/ZnS/α-Fe$_2$O$_3$ on surface of zinc oxides [32]. The direct band gap energy was calculated from the Tauc relation:

$$(\alpha h\upsilon)^2 = P(E_g - h\upsilon) \tag{3}$$

where α is the molar extinction coefficient, h is Plank constant, υ is the frequency of light, E_g is the bad gap energy, and P is the arbitrary constant. The linear part of the $(\alpha h\upsilon)^2$ versus $h\upsilon$ graph (Fig. 5(b)) was used to calculate the band gap values. The intercept of the tangent at the x-axis gives the band gap values, which are found to be 3.0, 2.85 and 2.65 eV for ZnO, ZnO/ZnS and ZnO/ZnS/α-Fe$_2$O$_3$ materials, respectively.

Room temperature PL spectra of ZnO, ZnO/ZnS, and ZnO/ZnS/α-Fe$_2$O$_3$ nanocomposites, recorded at an excitation wavelength of 325 nm, are shown in Fig. 6. In the PL spectrum of ZnO, the peak at 393 nm in the ultraviolet region corresponds to near-band-edge emission, due to radiative recombination of electrons in the conduction band and holes in the valance band. This band is red-shifted at 396 nm in the case of ZnO/ZnS and

further at 405 nm in the case of ZnO/ZnS/α-Fe$_2$O$_3$ in ultraviolet region. Meanwhile, the intensity of UV peak decreases successively from ZnO to ZnO/ZnS, and further from ZnO/ZnS to ZnO/ZnS/α-Fe$_2$O$_3$, in ultraviolet region, indicating that the rate of recombination of electron−holes slows down in ZnO/ZnS compared with ZnO and further in ZnO/ZnS/α-Fe$_2$O$_3$ compared with ZnO/ZnS. It has been reported previously that the incorporation of metal or non-metal ions (like carbon and iron) in the ZnO host significantly decreases the UV emission intensity [10,33].
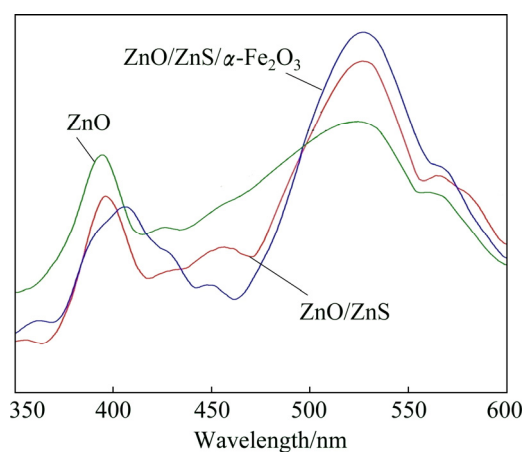
Fig. 6 PL spectra of ZnO, ZnO/ZnS and ZnO/ZnS/α-Fe$_2$O$_3$ nanocomposites

Various secondary visible emission peaks like blue, green, yellow, orange and red have been reported in pure ZnO NPs. Though extensive efforts have been made on visible emission of ZnO, their origin is highly controversial and still a matter of debate. In PL spectra of ZnO, the secondary peaks in the visible region are observed at 425 nm (2.92 eV) and 449 nm (2.76 eV) corresponding to blue emission, the peaks at 528 nm (2.35 eV) corresponding to green emission while the peak at 570 nm (2.18 eV) corresponding to yellow emission. A large number of reports revealed that the visible emissions are related to several intrinsic defects in ZnO materials. These defects include zinc vacancies (V_{Zn}), oxygen vacancies (V_O), interstitial zinc (Zn_i), interstitial oxygen (O_i) and antisite oxygen due to substitution of oxygen at zinc position (O_{Zn}) [34]. The energy levels of the intrinsic defects in ZnO have been computed theoretically and summarized in various reports [35,36].

The blue emission at 425 nm (2.92 eV) originated either due to transition from interstitial zinc (Zn_i) level to the valance band (VB) or transition from the bottom of the conduction band to interstitial oxygen (O_i) level [36]. Taking consideration of similarity between photoluminescence behavior of ZnS and ZnO, MAHAMUNI et al [37] stated that the emission at

420 nm is due to transition from conduction band to O_i levels of ZnO. Thus, the emission peak observed at 422 nm in our study is attributed to the transition of electrons from the bottom of conduction band to the O_i levels, whereas emission peak at 442 nm can be ascribed to the energy of transition of electron from Zn_i to VB. The other blue emission at 449 nm (2.76 eV) can be assigned to the energy of transition of electron from Zn_i to V_{Zn}, based on report in Ref. [36]. Previous works revealed that the green emission of ZnO is originated from several defects such as singly ionized oxygen vacancy $V_O^\bullet$, $V_O^{\bullet\bullet}$, Zn_i, V_{Zn} and O_{Zn} [25,38]. VANHEUSDEN et al [39] reported that the green emission in ZnO is originated due to the recombination of electrons in singly ionized oxygen vacancy with photo-excited holes in the valence band. ZHENG et al [25] demonstrated that green emission at 527 nm is attributed to the oxygen vacancy ($V_O^{\bullet\bullet}$) and interstitial oxygen (O_i). In this work, the position of green emission peak (at 527 nm) and intensity matched with that report, indicating that it is originated due to surface oxygen vacancy ($V_O^{\bullet\bullet}$) and interstitial oxygen (O_i). The yellow/orange emission, observed at 570 nm in ZnO, is due to the excess of interstitial oxygen (O_i) [25,40].

The intensity of UV peak of ZnO decreased in ZnO/ZnS and further in ZnO/ZnS/α-Fe$_2$O$_3$ conjuagate systems, whereas the intensities of green and yellow emissions have shown the reverse order. The peak positions of visible emissions shifted slightly in ZnO/ZnS and ZnO/ZnS/α-Fe$_2$O$_3$ as compared to ZnO. This indicates that the recombination rate of electron−holes is restrained while the levels of surface oxygen vacancy ($V_O^{\bullet\bullet}$) and interstitial oxygen (O_i) increase due to the addition of ZnS to ZnO and further by the addition of ZnS/α-Fe$_2$O$_3$ to ZnO.

Contaminant photodegradation capability of the above synthesized ZnO, ZnO/ZnS, and ZnO/ZnS/α-Fe$_2$O$_3$ photocatalysts was evaluated by recording photodegradation behavior of dye methyl orange (MeO). In the present study, continuous air bubbling was done to ensure the presence of sufficient amount of O$_2$, which was used as oxidizing agent. Figures 7(a)−(c) show the variation in the UV−visible absorbance spectra of MeO solution (50 mg/L) with irradiation time in the presence of ZnO, ZnO/ZnS, ZnO/ZnS/α-Fe$_2$O$_3$ photocatalysts, respectively.

Figure 8 shows the degradation extent of samples ZnO, ZnO/ZnS and ZnO/ZnS/α-Fe$_2$O$_3$ under visible light irradiation for 35 min. It is evident from the spectra that the photodegradation capacity of ZnO/ZnS/α-Fe$_2$O$_3$ is
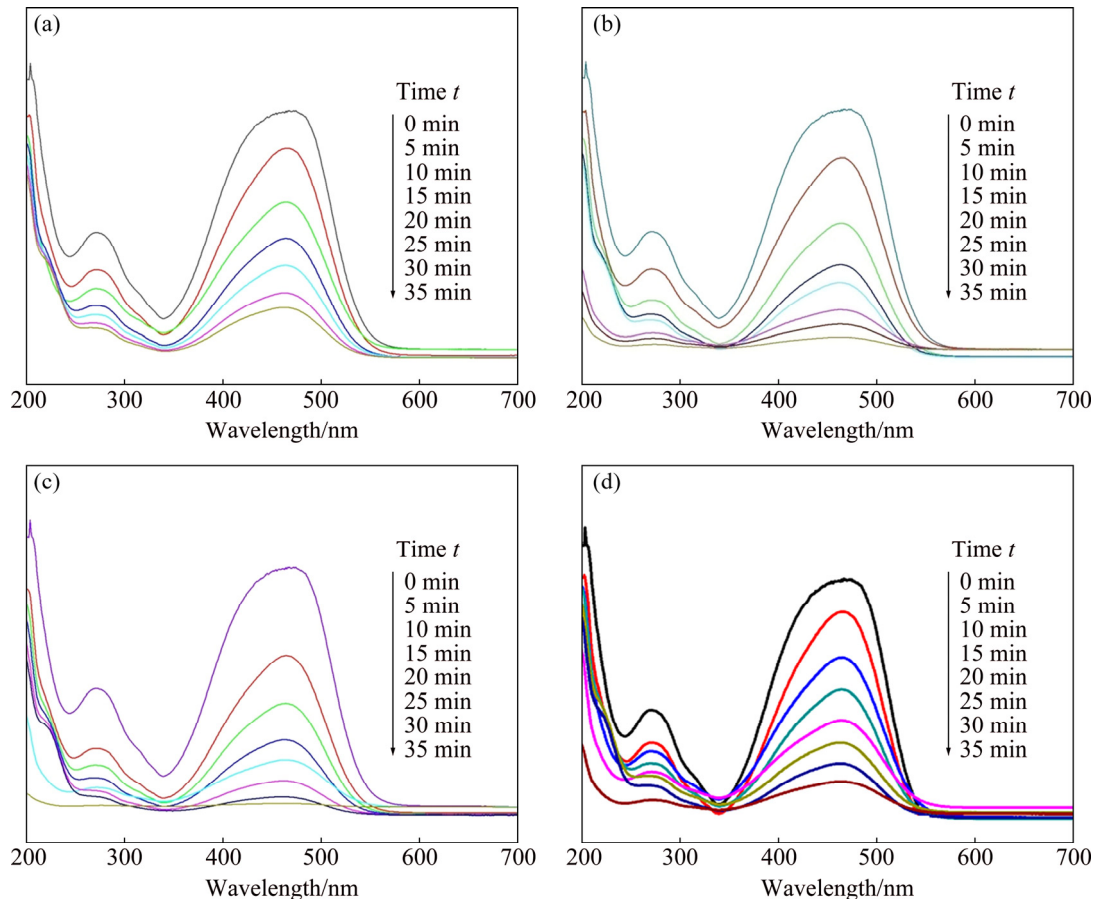
Fig. 7 Absorption spectra of MeO solution (100 mL, 50 mg/L) in the presence of 0.2 g ZnO (a), 0.2 g ZnO/ZnS (b) and 0.2 g ZnO/ZnS/α-Fe$_2$O$_3$ (c) and recycled ZnO/ZnS/α-Fe$_2$O$_3$ (d) materials
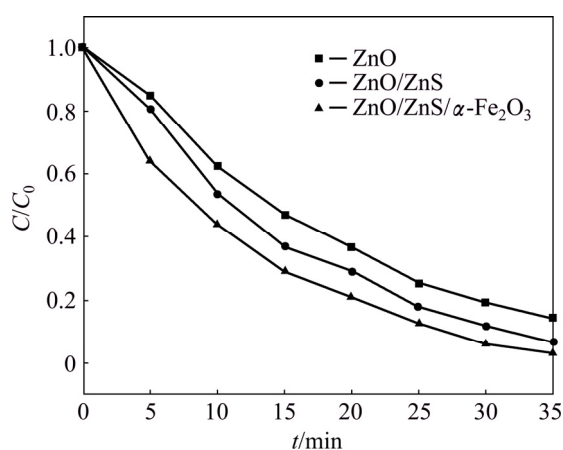
Fig. 8 Extent of degradation of MeO in the presence of ZnO, ZnO/ZnS and ZnO/ZnS/α-Fe$_2$O$_3$ catalysts

the highest and that of ZnO is the lowest, while in the case of ZnO/ZnS, it lies between ZnO and ZnO/ZnS/ α-Fe$_2$O$_3$ for degradation of MeO. Approximately 76% degradation of dye MeO has been found using ZnO as photocatalyst, while 85% degradation of dye has been observed using ZnO/ZnS nanocomposites. Almost complete degradation of adsorbed dye molecules (~97.55%) took place within 35 min using ZnO/ZnS/ α-Fe$_2$O$_3$ nanocomposite. 17.9% addition of ZnS to ZnO increased the degradation of MeO from 76% to 85% while addition of 40.93% α-Fe$_2$O$_3$ to ZnO/ZnS increased degradation from 85% to 97.55%. These data indicate that the addition of ZnS to ZnO plays better role in comparison of addition of α-Fe$_2$O$_3$ to ZnO/ZnS for degradation of dye MeO. However, the addition of α-Fe$_2$O$_3$ to the ZnO/ZnS has importance in another way, that is, the photocatalyst ZnO/ZnS/α-Fe$_2$O$_3$ can be easily recycled by magnetic adsorption. Hence, the ZnO/ZnS/ α-Fe$_2$O$_3$ is suitable and efficient photocatalyst for the degradation of MeO. In order to estimate the reusability of the tertiary ZnO/ZnS/α-Fe$_2$O$_3$ composites, these materials were recycled and washed several times with distilled water and dried at 100 °C. The regenerated ZnO/ZnS/α-Fe$_2$O$_3$ was reused and the degradation efficiency was measured to be 75% (Fig. 7(d)).

It is shown that the phoptocatalytic efficiency of semiconductor photocatalysts depends on various properties like band gap, phase/crystal structure, particle size, shape, surface area, surface defects and the presence of bound molecules on the surface [32,41].

The photocatalytic activity of ZnO, ZnO/ZnS and ZnO/ZnS/α-Fe$_2$O$_3$ has a direct correlation with surface area. The higher the surface area of which the catalyst possesses, the more the reactants (like O$_2$, OH$^-$ and MeO molecules) should be adsorbed on its surface, thus leading to higher photocatalytic activity. The photocatalytic activity for ZnO/ZnS/α-Fe$_2$O$_3$ is the

highest because its surface area is the highest (17.0 m^2/g), for ZnO, it is the lowest because the surface area of the sample is the lowest (14.37 m^2/g) while in case of ZnO/ZnS, it lies between those of two samples, because the surface area of ZnO/ZnS (15.96 m^2/g) lies between those of ZnO/ZnS/α-Fe$_2$O$_3$ and ZnO. The above data confirm that the photocatalytic activity of the materials have a direct correlation with the surface area of the photocatalysts [42], along with the crystallinity of the materials. The band gap energy of ZnO is too high to be excited by visible light; however, photocatalytic efficiency of ZnO is supposed to be dye-sensitized [33]. The band gap of ZnO can be manipulated to such an extent where visible light induced photocatalysis could take place effectively. Such modification can be achieved by doping or by the addition of other semiconductors to ZnO to make heterostructures like ZnO/ZnS and ZnO/ZnS/α-Fe$_2$O$_3$. Figure 5(b) shows that the band gap of pure ZnO (3.0 eV) is lowered to 2.85 eV in ZnO/ZnS and further to 2.65 eV in ZnO/ZnS/α-Fe$_2$O$_3$. The improvement of photocatalytic activity of ZnO/ZnS and ZnO/ZnS/α-Fe$_2$O$_3$ could be achieved due to the decrease of band gap values, since these are now effective in visible light.

The fact that the synthesized photocatalysts adsorb significantly more dye during the reaction, suggests a possible adsorption−desorption mechanism. Visible light irradiation generates an electron−hole pair on the surface of the above prepared ZnO, ZnO/ZnS, and ZnO/ZnS/ α-Fe$_2$O$_3$ catalysts. The electron-hole pair enables the formation of some intermediate radicals such as hydroxyl radicals, hydroperoxyl radicals and superoxide radical anions in the catalytic solution by their interaction with water and oxygen from the supplied air. Continuous air bubbling facilitates the formation of these radicals, mainly the hydroxyl radicals, which participate directly in the oxidative photodegradation of dye molecules. As the degradation involves adsorption-followed reaction, the adsorbed dye molecules can easily interact with the photo-generated oxidizing radical species, resulting in the degradation of dye. The high photocatalytic activity of ZnO/ZnS and ZnO/ZnS/α-Fe$_2$O$_3$ may be due to the diminishing of the recombination of electron−hole pairs in these materials and hence encouraging their catalytic activity. In PL spectra (Fig. 6), the intensity of UV peak of ZnO/ZnS is significantly lowered than that of ZnO while in ZnO/ZnS/α-Fe$_2$O$_3$, the intensity is further decreased. The decrease of intensity of UV emission peak is attributed to the decrease of recombination of electrons and holes, which in turn indicates the increase of rate of photocatalytic reaction. Thus, photocatalytic efficiency of ZnO/ZnS/α-Fe$_2$O$_3$ is the highest and that of ZnO is the lowest while in the case of ZnO/ZnS, it lies between ZnO and ZnO/ZnS/α-Fe$_2$O$_3$ for the degradation

of MeO. Moreover, the visible emissions revealed the existence surface oxygen defects, which act as electron acceptor. For instance, the oxygen vacancies ($V_O^{\cdot\cdot}$) work as electron acceptor and can temporarily trap photogenerated electrons in the conduction band while interstitial oxygen defects (O_i) trap the holes in valance band, resulting in retardation of electron−holes recombination. The higher the levels of $V_O^{\cdot\cdot}$ and O_i defects are, the higher the trapping of electrons and holes takes place on the surface of catalyst. Further, the higher the BET surface area is, the more the $V_O^{\cdot\cdot}$ and O_i defects are, resulting in higher photocatalytic activity. Since the surface area follows the trend of ZnO/ZnS/α-Fe$_2$O$_3$> ZnO/ZnS>ZnO, the amount of $V_O^{\cdot\cdot}$ and O_i defects follows the same trend [33]. In the PL spectra the intensity of green as well as yellow emissions increased successively from ZnO to ZnO/ZnS and further from ZnO/ZnS to ZnO/ZnS/α-Fe$_2$O$_3$, indicating the amount of $V_O^{\cdot\cdot}$ and O_i defects increased successively from ZnO to ZnO/ZnS and further from ZnO/ZnS to ZnO/ZnS/ α-Fe$_2$O$_3$. In fact, a large amount of $V_O^{\cdot\cdot}$ and O_i defects present in ZnO/ZnS and ZnO/ZnS/α-Fe$_2$O$_3$ function as trappers for electrons in the conduction band and holes in the valance band, thus resulting in the increasing rate of recombination of electrons and holes and increasing rate of photocatalysis in the presence of ZnO/ZnS to ZnO/ZnS/α-Fe$_2$O$_3$ nanocomposites.

The photocatalytic degradation of MeO under visible light irradiation using ZnO, ZnO/ZnS and ZnO/ZnS/α-Fe$_2$O$_3$ materials is an example of heterogeneous catalysis and these reactions seldom follow proper rate law model and hence it is inherently difficult to formulate rate equation from the observed data. However, it has been widely accepted that these reactions can be studied using Langmuir Hinshelwood (LH) model [43].

Applying the Langmuir Hinshelwood model for determining the oxidation rate of the photocatalysis of dye (r):

$$r = -\frac{\mathrm{d}C}{\mathrm{d}t} = \frac{-kKC}{1+KC} \tag{4}$$

where k is the rate constant, C is the concentration of dye, K is the adsorption constant of the dye, and t is the illumination time. Integrating Eq. (4), the rate law can be rearranged as

$$\ln(C/C_0) = -kt \tag{5}$$

where C_0 is the initial concentration of dye solution, C the concentration after time t and k is the rate constant. A graph between $\ln(C/C_0)$ versus t has been plotted (Fig. 9), where rate constant k can be determined by the slope of fitting curve. From Fig. 9, the rate constant values for ZnO, ZnO/ZnS and ZnO/ZnS/α-Fe$_2$O$_3$

catalysts have been determined to be 0.057, 0.076 and 0.082 min^{-1}, respectively. The results indicate that ZnO/ZnS/α-Fe$_2$O$_3$ is an excellent photocatalyst and the photocatalytic activity of these materials follows the following trend: ZnO/ZnS/ α-Fe$_2$O$_3$>ZnO/ZnS>ZnO for the degradation of dye MeO.
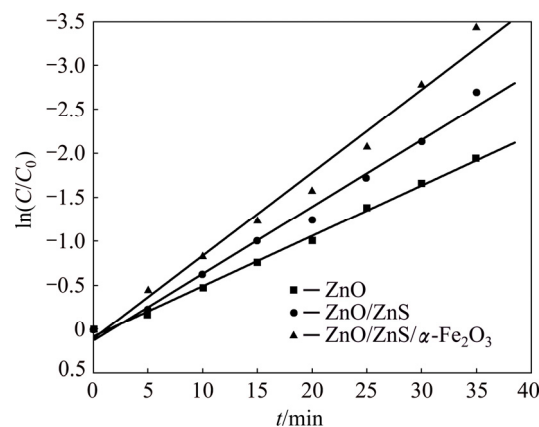

Fig. 9 Pseudo first order kinetics for degradation MeO in the presence of ZnO, ZnO/ZnS and ZnO/ZnS/α-Fe$_2$O$_3$ catalysts

4 Conclusions

In summary, ZnO nanoparticles, ZnO/ZnS and ZnO/ZnS/α-Fe$_2$O$_3$ composites have been successively synthesized by homogeneous precipitation method. The gradual three-step methodology may provide a promising technique for the synthesis of hybrid nanocomposites. XRD and SEM studies revealed a hexagonal wurtzite, sheet-like and needle-like acicular structure of ZnO, ZnO/ZnS and ZnO/ZnS/α-Fe$_2$O$_3$ nanocomposites with respective crystallite sizes of 120, 84 and 110 nm at a calcination temperature of 600 °C. The photocatalytic activity results revealed that the ZnO, ZnO/ZnS, and ZnO/ZnS/α-Fe$_2$O$_3$ nanocomposites formed by calcination at 600 °C are effective photocatalysts, and ZnO/ZnS/ α-Fe$_2$O$_3$ has the highest and ZnO has the lowest photocatalytic activity for the degradation of methyl orange. The UV−visible absorption showed that the band gap of ZnO (3.1 eV) is decreased to 2.85 eV for ZnO/ZnS and further to 2.65 eV for ZnO/ZnS/α-Fe$_2$O$_3$ nanocomposites. Therefore, photocatalytic activity of ZnO/ZnS is higher than that of ZnO while that for ZnO/ZnS/α-Fe$_2$O$_3$ is the highest among the three samples for the degradation of MeO under visible light irradiation. PL spectral analysis indicated the successive decrease of rate of recombination of electron−hole from ZnO to ZnO/ZnS, and further from ZnO/ZnS to ZnO/ZnS/ α-Fe$_2$O$_3$. Thus, the increase of surface area, decrease of band gap and effective retardation of electron−hole recombination follow the trend ZnO/ZnS/α-Fe$_2$O$_3$> ZnO/ZnS>ZnO for the degradation of MeO under visible light.

References

[1] VERENICH S, KALLAS J. Wet oxidation lumped kinetic model for wastewater organic burden biodegradability prediction [J]. Environmental Science & Technology, 2002, 36: 3335−3339.

[2] ASAHI R, MORIKAWA T, OHWAKI T, AOKI K, TAGA Y. Visible-light photocatalysis in nitrogen-doped titanium oxides [J]. Science, 2001, 293: 269−271.

[3] SELVAM V, KUMAR P S, KRISHNAN G N, ANDAVAN G S. Photocatalytic degradation of organic contaminants by gC$_3$N$_4$/EPDM nanocomposite film: Viable, efficient and facile recoverable [J]. Materials Science and Engineering C, 2018, 84: 188−194.

[4] CHEN X, MAO S. Titanium dioxide nanomaterials: Synthesis, properties, modifications, and applications [J]. Chemical Reviews, 2007, 107: 2891−2959.

[5] TONG H, OUYANG S, BI Y P, UMEZAWA N, OSHIKIRI M, YE J. Nano-photocatalytic materials: Possibilities and challenges [J]. Advanced Materiales, 2012, 24: 229−251.

[6] LIU Y, XIE C, LI J, ZOU T, ZENG D. New insights into the relationship between photocatalytic activity and photocurrent of TiO$_2$/WO$_3$ nanocomposite [J]. Applied Catalysis A: General, 2012, 433: 81−87.

[7] SHWETHARANI R, JYOTHI M, LAVEENA P, GEETHA BALAKRISHNA R. Photoactive titania float for disinfection of water; evaluation of cell damage by bioanalytical techniques [J]. Photochemistry and Photobiology, 2014, 90: 1099−1107.

[8] PANDEY G, DIXIT S, SHRIVASTAVA A K. Role of additives; sodium dodecyl sulphate and manganese chloride on morphology of Zn$_{1-x}$Mn$_x$O nanoparticles and their photoluminescence properties [J]. Materials Chemistry and Physics, 2014, 147: 423−432.

[9] BAI X, WANG L, ZONG R, LV Y, SUN Y, ZHU Y. Performance enhancement of ZnO photocatalyst via synergic effect of surface oxygen defect and graphene hybridization [J]. Langmuir, 2013, 29: 3097−3105.

[10] FENG X, GUO H, PATEL K, ZHOU H, LOU X. High performance, recoverable Fe$_3$O$_4$ ZnO nanoparticles for enhanced photocatalytic degradation of phenol [J]. Chemical Engineering Journal, 2014, 244: 327−334.

[11] YANG Y C, LIU Y, WEI J H, PAN C X, XIONG R, SHI J. Electrospun nanofibers of p-type BiFeO$_3$/n-type TiO$_2$ hetero-junctions with enhanced visible-light photocatalytic activity [J]. RSC Advances, 2014, 4: 31941−31947.

[12] RAKSHIT T, MONDAL S, MANNA I, RAY S K. CdS-decorated ZnO nanorod heterostructures for improved hybrid photovoltaic devices [J]. ACS Applied Materials & Interfaces, 2012, 4: 6085−6095.

[13] GOMATHISANKAR P, HACHISUKA K, KATSUMATA H, SUZUKI T, FUNASAKA K, KUNIHIRO F, KANECO S. Enhanced photocatalytic hydrogen production from aqueous methanol solution using ZnO with simultaneous photodeposition of Cu [J]. International Journal of Hydrogen Energy, 2013, 38: 11840−11846.

[14] LI Z, SUN S, XU X, ZHENG B, MENG A. Photocatalytic activity and DFT calculations on electronic structure of N-doped ZnO/Ag nanocomposites [J]. Catalysis Communications, 2011, 12: 890−894.

[15] ZHANG S, WEI S H, ZUNGER A. Microscopic origin of the phenomenological equilibrium "doping limit rule" in n-type III−V semiconductors [J]. Physical Review Letters, 2000, 84: 1232−1235.

[16] CUN W, JINCAI Z, XINMING W, BIXIAN M, GUOYING S, PINGAN P, JIAMO F. Preparation, characterization and photocatalytic activity of nano-sized ZnO/SnO$_2$ coupled photocatalysts [J]. Applied Catalysis B: Environmental, 2002, 39: 269−279.

[17] QINGÁLU G. Enhanced photocatalytic hydrogen evolution by prolonging the lifetime of carriers in ZnO/CdS heterostructures [J]. Chemical Communications, 2009, 23: 3452−3454.

[18] MAEDA K, TAKATA T, HARA M, SAITO N, INOUE Y, KOBAYASHI H, DOMEN K. GaN: ZnO solid solution as a photocatalyst for visible-light-driven overall water splitting [J]. Journal of the American Chemical Society, 2005, 127: 8286−8287.

[19] LAI Y, MENG M, YU Y. One-step synthesis, characterizations and mechanistic study of nanosheets-constructed fluffy ZnO and Ag/ZnO spheres used for Rhodamine B photodegradation [J]. Applied Catalysis B: Environmental, 2010, 100: 491−501.

[20] LEE M, YONG K. Highly efficient visible light photocatalysis of novel CuS/ZnO heterostructure nanowire arrays [J]. Nanotechnology, 2012, 23: 194014.

[21] LAHIRI J, BATZILL M. Surface functionalization of ZnO photocatalysts with monolayer ZnS [J]. The Journal of Physical Chemistry C, 2008, 112: 4304−4307.

[22] ZHANG J, YU J, ZHANG Y, LI Q, GONG J R. Visible light photocatalytic H2-production activity of CuS/ZnS porous nanosheets based on photoinduced interfacial charge transfer [J]. Nano Letters, 2011, 11: 4774−4779.

[23] LIU C, YANG D, JIAO Y, TIAN Y, WANG Y, JIANG Z. Biomimetic synthesis of TiO$_2$−SiO$_2$−Ag nanocomposites with enhanced visible-light photocatalytic activity [J]. ACS Applied Materials & Interfaces, 2013, 5: 3824−3832.

[24] LIU S, WANG X, ZHAO W, WANG K, SANG H, HE Z. Synthesis, characterization and enhanced photocatalytic performance of Ag$_2$S-coupled ZnO/ZnS core/shell nanorods [J]. Journal of Alloys and Compounds, 2013, 568: 84−91.

[25] ZHENG Y, ZHENG L, ZHAN Y, LIN X, ZHENG Q, WEI K. Ag/ZnO heterostructure nanocrystals: Synthesis, characterization, and photocatalysis [J]. Inorganic Chemistry, 2007, 46: 6675−6682.

[26] TORABI A, STAROVEROV V N. Band gap reduction in ZnO and ZnS by creating layered ZnO/ZnS heterostructures [J]. The Journal of Physical Chemistry Letters, 2015, 6: 2075−2080.

[27] SAHA S, SARKAR S, PAL S, SARKAR P. Tuning the energy levels of ZnO/ZnS core/shell nanowires to design an efficient nanowire-based dye-sensitized solar cell [J]. The Journal of Physical Chemistry C, 2013, 117: 15890−15900.

[28] PANDEY S K, PANDEY S, PARASHAR V, YADAV R, MEHROTRA G, PANDEY A C. Band gap engineering of colloidal zinc oxysulfide via lattice substitution with sulfur [J]. Nanoscale, 2014, 6: 1602−1606.

[29] SONKER R K, SABHAJEET S R, YADAV B C. TiO$_2$−PANI nanocomposite thin film prepared by spin coating technique working as room temperature CO$_2$ gas sensing [J]. Journal of Materials Science: Materials in Electronics, 2016, 11: 11726−11732.

[30] BARICK K C, SINGH S, ASLAM M, BAHADUR D. Porosity and photocatalytic studies of transition metal doped ZnO nanoclusters [J]. Microporous and Mesoporous Materials, 2010, 134: 195−202.

[31] GAWADE V V, GAVADE N L, SHINDE H M, BABAR S B, KADAM A N, GARADKAR K M. Green synthesis of ZnO nanoparticles by using calotropis procera leaves for the photodegradation of methyl orange [J] Journal of Materials Science: Materials in Electronics, 2017, 28: 1−7.

[32] SAARENPÄÄ H, SARIOLA-LEIKAS E, PYYMAKI P A, KONTIO J M, EFIMOV A, HAYASHI H, LIPSANEN H, IMAHORI H, LEMMETYINEN H, TKACHENKO N V. Self-assembled porphyrins on modified zinc oxide nanorods: Development of model systems for inorganic−organic semiconductor interface studies [J]. The Journal of Physical Chemistry C, 2012, 116: 2336−2343.

[33] ZHANG X, QIN J, HAO R, WANG L, SHEN X, YU R, LIMPANART S, MA M, LIU R. Carbon-doped ZnO nanostructures: Facile synthesis and visible light photocatalytic applications [J]. The

Journal of Physical Chemistry C, 2015, 119: 20544−20554.

[34] SABRI N S, YAHYA A K, TALARI M K. Emission properties of Mn doped ZnO nanoparticles prepared by mechanochemical processing [J]. Journal of Luminescence, 2012, 132: 1735−1739.

[35] DJURISIC A K, LEUNG Y H, TAM K, DING L, GE W, CHEN Y, GWO S. Green, yellow, and orange defect emission from ZnO nanostructures: Influence of excitation wavelength [J]. Applied Physics Letters, 2006, 88: 103107.

[36] PENGSHOU X, YUMING S, CHAOSHU S, FAQIANG X, HAIBIN P. Electronic structure of ZnO and its defects [J]. Science in China Series A: Mathematics, 2001, 44: 1174−1181.

[37] MAHAMUNI S, BORGOHAIN K, BENDRE B S. Spectroscopic and structural characterization of electrochemically grown ZnO quantum dots [J]. Journal of Applied Physics, 1999, 85: 2861−2665.

[38] HITKARI G, SINGH S, PANDEY G. Structural, optical and photocatalytic study of ZnO and ZnO−ZnS synthesized by chemical method [J]. Nano-Structures & Nano-Objects, 2017, 12: 1−9.

[39] VANHEUSDEN K, SEAGER C, WARREN W, TALLANT D, VOIGT J. Correlation between photoluminescence and oxygen vacancies in ZnO phosphors [J]. Applied Physics Letters, 1996, 68: 403−405.

[40] ELILARASSI R, CHANDRASEKARAN G. Mater. Effect of annealing on structural and optical properties of zinc oxide films [J]. Materials Chemistry and Physics, 2010, 121: 378−384.

[41] JIAO Y, LIU Y, QU F, UMAR A, WU X. Visible-light-driven photocatalytic properties of simply synthesized α-iron (III) oxide nanourchins [J]. Journal of Colloid and Interface Science, 2015, 451: 93−100.

[42] POURETEDAL H, KADKHODAIE A. Synthetic CeO_2 nanoparticle catalysis of methylene blue photodegradation: Kinetics and mechanism [J]. Chinese Journal of Catalysis, 2010, 31: 1328−1334.

[43] DU E, ZHANG Y X, ZHENG L. Photocatalytic degradation of dimethyl phthalate in aqueous TiO_2 suspension: A modified Langmuir–Hinshelwood model [J]. Reaction Kinetics and Catalysis Letters, 2009, 97: 83−90.

ZnO、ZnO/ZnS 和 ZnO/ZnS/α-Fe₂O₃ 纳米复合材料的光致发光行为及可见光催化活性

Gaurav HITKARI, Sandhya SINGH, Gajanan PANDEY

Sophisticated Instrumentation Laboratory, Department of Applied Chemistry,

School for Physical Science, Babasaheb Bhimrao Ambedkar University, Lucknow-226025 (U.P.), India

摘　要：为了获得用于染料甲基橙(MEO)降解的高效、经济、易得的光催化剂，采用简单的化学合成法在水溶液介质中制备 ZnO、ZnO/ZnS 和 ZnO/ZnS/α-Fe₂O₃ 纳米复合材料。利用 X 射线衍射(XRD)和 BET 技术测定合成材料的物相、结晶度、表面结构和表面行为。X 射线衍射结果表明，ZnO、ZnO/ZnS 和 ZnO/ZnS/α-Fe₂O₃ 纳米材料结晶良好。根据 XRD 谱中各峰的强度，确定纳米复合材料的组成。BET 分析表明，所制备的材料具有介孔行为、IV 型(吸附脱附)曲线和 H4 型迟滞现象。3 种材料中，ZnO/ZnS/α-Fe₂O₃ 复合材料的比表面积最大。利用紫外−可见光谱分析，测定材料的带隙能，光致发光光谱(PL)则用来确定材料的发射行为和表面缺陷。在 PL 光谱中，ZnO/ZnS 的紫外峰强度比 ZnO 的低，且 ZnO/ZnS/α-Fe₂O₃ 的紫外峰强度更低。与 ZnO 相比，ZnO/ZnS 的可见发射光谱强度增大，且 ZnO/ZnS/α-Fe₂O₃ 的可见发射光谱强度比 ZnO/ZnS 的更大。所合成的材料被用作染料甲基橙降解的光催化剂。光降解数据表明，3 种染料甲基橙降解的光催化剂中 ZnO/ZnS/α-Fe₂O₃ 是最佳的。紫外光发射峰强度的降低和可见光发射强度的增大导致电子和空穴复合减少，因而使得 ZnO/ZnS/α-Fe₂O₃ 具有最高的光催化活性。

关键词：纳米复合材料；ZnO；ZnS；α-Fe₂O₃；煅烧；光学性质；光催化活性

(Edited by Wei-ping CHEN)